Turbid water sun glint removal for high resolution sensors without SWIR

Héloïse Lavigne*[a], Quinten Vanhellemont[a], Kevin Ruddick[a], Dieter Vansteenwegen[b]
[a]Royal Belgian Institute of Natural Sciences, rue Vautierstraat 29, 1000 Brussels, Belgium
[b]Flanders Marine Institute (VLIZ), Wandelaarkaai 7, 8400 Ostend, Belgium

ABSTRACT

The loss of satellite data over water because of sun glint contamination represents a high cost financially and scientifically. Although many glint removal algorithms have been developed, glint contamination can remain problematic, especially in turbid waters. In the present study, we propose a correction for sun glint in turbid waters in the absence of SWIR bands. This method could for example be applied to imagery from the Pléiades and Planetscope constellations.

Our method has been developed and tested using (1) in situ multi-angle measurements of surface reflectance collected with a PANTHYR autonomous hyperspectral radiometer deployed near Ostend, and (2) a set of metre-scale Pléiades stereo imagery taken in the Belgian coastal zone, with one image of the stereo pair looking into the sun glint and one looking away from the sun glint. The method uses combinations of spectral bands for which a linear relationship is observed in water reflectance, and a constant band ratio for glint reflectance directly calculated from the glinted image. To be adapted to a high range of turbidity conditions, a switching approach between band combinations is used. Glint removal correction was successfully applied in association with the ACOLITE Dark Spectrum Fitting (DSF) atmospheric correction. Results show a good performance in terms of glint removal, and the average overestimation is reduced to less than 20 % in visible bands.

Keywords: sun glint, Pléiades, water reflectance, ocean colour, turbid waters

1 INTRODUCTION

Sun glint is the specular reflection of directly transmitted sunlight at the air-water interface. For a flat sea, sun glint intensity depends on sun and sensor position as if the sea were a mirror. Sun glint is maximum when the azimuthal angle between sensor and sun position is 180° and when sensor and sun zenith angles are equal but it depends also on wind intensity as a rough sea will tend to spread the sun glint signal over a wider range of angles.

Although some satellite instruments (i.e. SeaWiFS, OCTS and CZCS) were able to tilt 20° along-track from nadir to minimize sun glint, most spaceborne instruments do not have such tilting capability and glint avoidance is therefore not possible. Particularly for narrow swatch near-nadir pointing instruments, sun glint contamination often makes accurate retrieval of water reflectance signal impossible. Imagery lost to sun glint represents a high cost both financially and scientifically. For instance, Hochberg et al. [1] reported a significant amount of IKONOS images of coral reefs badly contaminated by glint in its dataset and Steinmetz et al. [2] raised the problem of strong glint contamination in MERIS images acquired in tropical latitudes.

To avoid the simple masking and removal of glint contaminated pixels, sun glint correction algorithms have been developed. Sun glint correction algorithms aim to retrieve the quantity of radiance reaching the sensor which is due to glint and to subtract it. There are two main classes of methods depending on the spatial resolution of satellite sensors [3]. For low to moderate spatial resolution sensors (from 100m) the statistical model of Cox and Munk [4] is typically used. This model, which depends on wind speed and direction, calculates the fraction of water surface facets that are oriented in a direction that causes glint. This approach has been used for SeaWiFS [5] and MERIS [6] atmospheric corrections and works well for low to moderate sun glint but fails to correct the brightest glint areas. When sensor spatial resolution is high and wave patterns are similar to or larger than a pixel size, the spatially-averaged approach of the Cox and Munk [4] model does not apply anymore. In this case, models based on the extrapolation of the NIR signal to determine sun glint radiance are used. These models generally assume zero water leaving reflectance in NIR which is problematic for high turbid regions. For instance, Hedley et al. [7]selected deep water pixels in the image to parameterize the impact of glint in NIR

*hlavigne@naturalsciences.be

and VIS. More recently, Harmel et al. [8] proposed a pixel-based sun glint correction algorithm for Sentinel 2 SMI sensor based on SWIR reflectance. Assuming zero water reflectance in SWIR, the authors proposed to compute SWIR glint reflectance for all pixels. Then, from a known relationship between glint reflectance in SWIR and VIS spectral bands, glint is estimated in visible bands. To avoid the limitation of needing a zero water leaving reflectance in NIR or the availability of SWIR bands, Kutser et al. [9] proposed an algorithm based on the oxygen absorption feature in the atmosphere. However, this algorithm requires hyperspectral acquisition.

In the present study, we present a new methodology to correct sun glint in turbid water without NIR or SWIR zero water reflectance leaving assumption. The new method has been developed for the very high (meter-scale) spatial resolution sensor Pléiades. Pléiades-1 is a two-satellite constellation that provides multi-spectral imagery at 2.8 m spatial resolution in four broad bands (blue, green, red and NIR). With the development of commercial nano-satellites, the meter-scale imagery-based sensor with a few visible and NIR bands is expected to become more and more affordable (see for instance the Dove satellites of the Planetscope series, https://earth.esa.int/eogateway/missions/planetscope). Hence, solutions to resolve sun glint in turbid coastal regions and without a SWIR band are needed. The present methodology is based on spectral band combinations for which a linear relationship is observed in water reflectance, and a constant band ratio for glint reflectance directly calculated from the glinted images. Although it has been developed from Pléiades images, the concept has also been tested from in situ radiometric measurements performed in highly glinted waters.

In this paper, first the in situ radiometric measurements and Pléiades images used for algorithm development and testing are described. Then, the sun glint removal methodology is explained and results are presented and discussed in Section 4.

2 DATA AND METHODS

2.1 PANTHYR experiment

The in situ radiometric data used to test the present sun glint correction methodology were collected by an autonomous hyperspectral radiometers system named PANTHYR [10]. The PANTHYR system is deployed above water on the Blue Innovation Platform Research Tower 1 (51.2464°N, 2.9193°E), 500 m offshore of Ostend harbour in the Belgian Coastal Zone since December 2019 and has been previously used for validation of optical satellite products [11] and harmful algal bloom monitoring [12]. The PANTHYR system is composed of two TriOS/RAMSES radiometers for radiance and irradiance respectively mounted on a pan-and-tilt head which allows for continuous radiometric measurements at specified relative azimuth to sun. A standard acquisition protocol has been designed to estimate water reflectance. It lasts for about one minute and it is composed of 3 scans for spectral downwelling irradiance (E_d), 3 scans for downwelling radiance (L_d) and 11 scans for upwelling radiance (L_u), 3 more scans for downwelling radiance and 3 more scans for spectral downwelling irradiance. Measurements are performed every 20 min from sunrise to sunset for relative azimuth angles of 270◦ and 225◦ away from sun. Then, data are quality checked and water reflectance (ρ_w) is calculated as described in [11], based on [13].

For the sun glint experiment presented here, additional radiometric measurements were performed every 20 minutes in between two standard measurement protocols. A special "hotspot" protocol (Figure 1) was designed to measure upwelling radiance in the glint. This protocol consists of a "cycle" of 23 L_u measurements for view zenithal angles (VZA) ranging between 30° and 50° and relative azimuthal angle to sun (Φ) ranging between -20° and +20°. Each position was scanned 3 times, termed hereafter "set". In addition to L_u measurements, sky measurements (L_d) were performed for positions with Φ=+/-20° for VZA=40° and 50° (but not for VZA=30° because of mechanical angle limitations of the instrument). Finally, irradiance measurements (E_d) were performed at the beginning and end of the cycle. Because of platform geometry and sensor orientation, these measurements were acquired in the morning between 08:00 and 10:15 UTC.

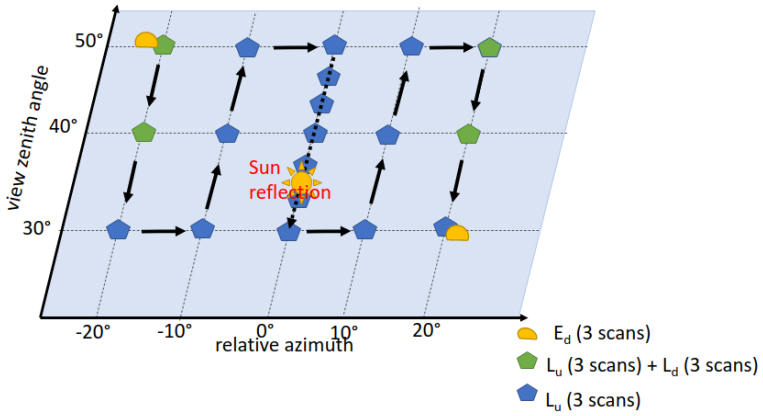

Figure 1. Schematic representation of the sampling protocol for the sun glint experiment. At 0° relative azimuth a scan is performed every 2° of from VZA=50° to VZA=30° (but is shown here only every 3.3°)

2.2 Data processing and quality control

First, only measurements performed with SZA between 25° and 55° were retained. Then, for each set of scans, the three replicates were compared. If standard deviation of radiance/irradiance at 550 nm over the 3 replicates is greater than 30% of the mean then data is rejected. A full cycle of measurements was considered as valid if (1) the two E_d measurements (collected at the beginning and end of the cycle) were valid and similar (less than 30% variation) and if (2) at least three measurements of L_d over the four were valid. To process a cycle, it was also required that a valid estimation of the water reflectance is available from the standard measurement protocol achieved just before the sun glint measurement protocol. The standard protocol quality control also ensures good sea and clear sky conditions [11].

Finally, an estimation of the surface reflectance corrected for sky glint (ρ_{surf}) was calculated from the following equation.

$$\rho_{surf} = \frac{\pi(L_u - \rho_{sky} L_d)}{E_d} \quad (1)$$

Where E_d is the mean average of all E_d spectra and L_d is the sky radiance showing lowest values among the four spectra measured. This lowest value has been chosen to avoid adding sun glint correction in the sky correction although it is not easy to separate these both elements from in situ measurements. In addition, again to avoid integrating sun glint correction into the sky reflectance correction, the Austin [14]Fresnel reflection coefficients were used for the air-water surface reflectance factor (ρ_{sky}) as they do not include sun glint effects contrary to the coefficients provided by Mobley [15]. Coefficients for a wind speed of 5 m s^{-1} were used. They vary from 0.0226 for a viewing angle of 30° to 0.0366 for a viewing angle of 50°. After this first processing step, 34 cycles were selected.

2.3 Calculation of glint spectra and post quality control

To obtain glint reflectance at bottom of the atmosphere (ρ_{glint}) from the PANTHYR measurements, water reflectance obtained from the standard protocol (ρ_{wSP}) was subtracted from ρ_{surf} . In (2) as we assume that angular variability of water reflectance between standard and hotspot geometries is negligible compared to the sun glint reflectance. These ρ_{glint} estimations were used for validation but also to apply an additional quality control.

$$\rho_{glint} = \rho_{surf} - \rho_{w_{SP}} \quad (2)$$

For additional quality control, the glint ratio between visible (VIS) spectral bands and NIR band has been explored. This ratio depends primarily on the ratio of the downward direct (T_{dir}) and diffuse (T_{diff}) transmittances of the atmosphere since the Fresnel reflectance at the water surface $r(\theta,\lambda)$ has low spectral variability: Equation(3).

$$\frac{\rho_{glint}(\lambda_{VIS})}{\rho_{glint}(\lambda_{NIR})} = \frac{T_{diff}(\lambda_{NIR})}{T_{diff}(\lambda_{VIS})} \cdot \frac{T_{dir}(\lambda_{VIS})}{T_{dir}(\lambda_{NIR})} \cdot \frac{r(\theta,\lambda_{VIS})}{r(\theta,\lambda_{NIR})} \quad (3)$$

Although $\rho_{glint}(\lambda_{VIS})/\rho_{glint}(\lambda_{NIR})$ varies air mass, a similar spectral shape is expected with increasing values from blue to NIR [16]. Hence, there is an additional quality control step aimed to check the relative homogeneity of $\rho_{glint}(\lambda_{VIS})/\rho_{glint}(\lambda_{NIR})$ within a same cycle. In practice, within a cycle, if the standard deviation of $\rho_{glint}(550)/\rho_{glint}(800)$ was higher than 0.05, the full cycle was deleted. Then, for each spectrum if the difference between the individual glint ratio at 550 nm and the cycle average was higher than 1.8 times the standard deviation, the spectrum was deleted (Figure 2). These deviations are due to incorrect sky glint correction because of non-optimal sky and water conditions. This QC resulted in the removal of 10 cycles and 46 individual spectra.

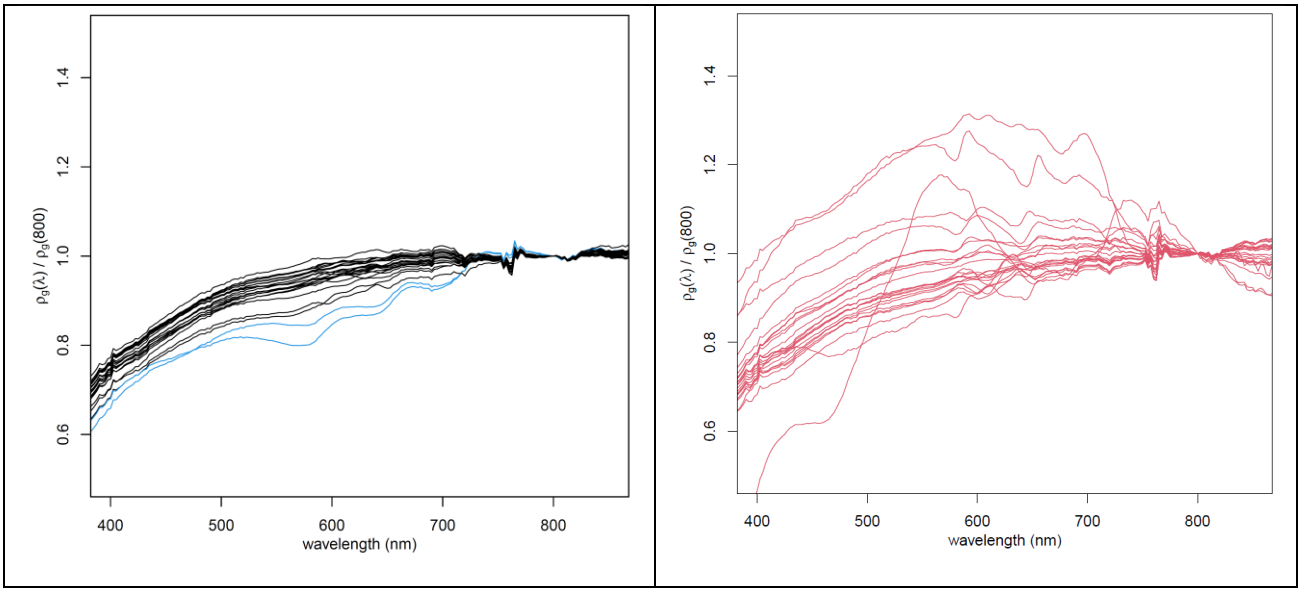

Figure 2. $\rho_{glint}(\lambda)/\rho_{glint}(800)$ as a function of λ for two cycles of measurements. Spectra in black have passed quality control, spectra in blue and red are eliminated individually (blue) or for the whole cycle (red). Left panel shows the cycle from 2022-08-10 at 09:20 UTC and right panel the cycle from 2022-08-13 at 09:40 UTC.

2.4 Pléiades satellite data

Pléiades is a meter-scale satellite with 4 spectral bands in visible and NIR at 2.8 m resolution and a panchromatic band at 0.7 m resolution which is not used here (Table 1). Imagery is typically resampled to 2 m and 0.5 m by the satellite operator. Pleiades acquisitions with the stereoscopic mode (dual-look) were ordered in spring 2020 from Airbus Defence and Space (intelligence-airbusds.com) to obtain a set of pairs of images with and without sun glint. Two test sites showing high turbidity were selected in the Belgian coastal zone: in and offshore from Ostend harbor (51.24°N, 2.92°E) and Zeebrugge harbor (51.35°N, 3.20°E).

Pléiades images have been processed for atmospheric correction with the Dark Spectrum Fitting (DSF) algorithm [17] available with the ACOLITE software (https://github.com/acolite/acolite/releases/tag/20221114.0). The DSF algorithm

was originally designed for very high-resolution sensors with few bands such as Pleiades although it has also been applied to high resolution sensors (e.g. Sentinel 2, Landsat 8, [18]) and moderate resolution sensors (Sentinel 3 OLCI [11]). For Pleiades processing, the algorithm assumes a) the atmosphere is homogeneous over the image and b) there exists at least one pixel for one spectral band with zero surface reflectance. In images with turbid waters, this dark pixel-band is generally on land. Hence, as explained by Vanhellemont [18], the retrieval of aerosol optical properties should not be impacted by sun glint but glint reflectance will remain in water reflectance retrieval and will have to be corrected in a separate step. This is verified when comparing results of the DSF algorithm between glinted and non-glinted images (Table 2) as we generally retrieve similar aerosol optical thickness (AOT) and aerosol models.

After atmospheric correction, to allow pixel by pixel comparison, non-glinted images were collocated to the glinted image with the nearest neighbor method. Then, 5 pairs of near-simultaneous (about 1-minute time difference) glinted and non-glinted Pléiades images were available for algorithm test and validation with the non-glinted images are considered as the reference.

Thereafter, the output of the DSF atmospheric correction is called $\rho_{surf}(\lambda)$ and is composed of the sum of water reflectance $\rho_w(\lambda)$ and glint reflectance $\rho_{glint}(\lambda)$ (glint reflectance being normalized by downwelling irradiance at bottom of atmosphere), similarly to the output of the PANTHYR in situ data processing. In DSF processing, the diffuse sky reflectance reflected at the air-water interface is computed analytically following Gordon et al. [19]. In the non-glinted images $\rho_{surf}(\lambda) = \rho_w(\lambda)$ and $\rho_{glint}(\lambda) = 0$.

Table 1. Pléiades-1 spectral specifications ([17])

Band	spectral range	Spatial resolution
Blue	450-520 nm	2.8 m
Green	520-600 nm	2.8 m
Red	630-690 nm	2.8 m
NIR	760-900 nm	2.8 m
panchromatic	450-900 nm	0.7 m

Table 2. Aerosol optical thickness (AOT) and model resulting from the DSF atmospheric correction processing on glinted and non-glinted Pléiades images. Each image has been processed individually.

date	**place**	**ID (time UTC)**	**glinted / non-glinted**	**AOT DSF**	**aerosol model**
2020-04-16	ZEEBRUGGE	11 12 45	glinted	0.4500	maritime
2020-04-16	ZEEBRUGGE	11 13 36	non-glinted	0.4376	maritime
2020-04-10	ZEEBRUGGE	11 09 22	glinted	0.3779	maritime
2020-04-10	ZEEBRUGGE	11 10 00	non-glinted	0.4000	maritime
2020-04-05	ZEEBRUGGE	10 57 58	glinted	0.2740	maritime
2020-04-05	ZEEBRUGGE	10 58 49	non-glinted	0.2700	maritime
2020-04-16	OSTEND	11 12 53	glinted	0.3648	maritime
2020-04-16	OSTEND	11 13 45	non-glinted	0.4646	maritime
2020-04-09	OSTEND	11 16 39	glinted	0.4109	maritime
2020-04-09	OSTEND	11 17 29	non-glinted	0.4225	maritime

2.5 Determination of glint ratio on Pléiades images

The glint ratio between visible spectral band and NIR ($GR_{VIS\ NIR}$, hereafter) are estimated separately for each glinted image without using information from the non-glinted images. Because in a 10x10km box variability in atmospheric conditions as well as viewing geometry can be considered as almost homogeneous, it is assumed that $GR_{VIS\ NIR}$ is constant over these small images. The methodology used for $GR_{VIS\ NIR}$ calculation is based on the hypothesis that on a macro-pixel (in practice 11x11 pixels), variability in $\rho_{surf}(\lambda)$ is mostly due to glint variability and not to the spatial variability of water reflectance. Hence, a constant water reflectance is assumed in a macro-pixel. From this assumption, the slope of the relationship calculated in a macro-pixel between VIS and NIR spectral bands equals $GR_{VIS\ NIR}$ (Figure 3). In practice, linear regression has been calculated at regular steps (a 11*11 pixel tile every 25 pixels vertically and horizontally, so not including all pixels of an image) to minimize computation time. Individual $GR_{VIS\ NIR}$ estimations were considered as valid if the coefficient of determination of the linear model (r^2) was higher than 0.65. Indeed, low r^2 values would indicate a too low variability in glint reflectance in the macro-pixel or a too high variability in water reflectance in the macro-pixel. Visual inspection of the spatial variability of individual $GR_{VIS\ NIR}$ values confirmed its spatial homogeneity (results not shown). The final $GR_{VIS\ NIR}$ estimation for an image was defined as the median of the series of individual estimations and is provided in Table 3. As expected, $GR_{blue\ VIS}$ is lower than $GR_{green\ NIR}$ which is lower than $GR_{red\ NIR}$.

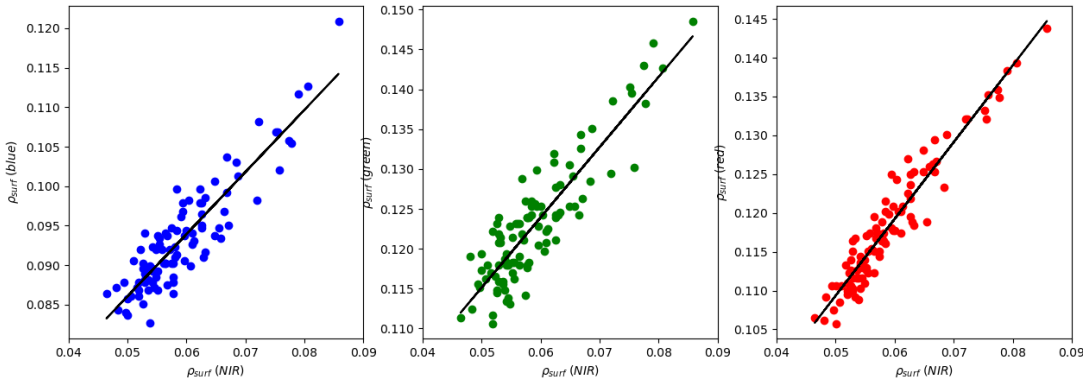

Figure 3. Surface reflectance in NIR and blue (left), green (middle) and red (right) bands for macro pixel tiles of 11x11 pixels extracted from the image ZE 2020-0-05. Black line shows the linear regressions with r^2 of 0.82, 0.80 and 0.92 for blue, green and red bands respectively.

Table 3. Results of the glint ratio calculation from macro-pixel linear regression method. Values in brackets are standard deviation.

Image reference	**GR red NIR**	**GR green NIR**	**GR blue NIR**
OS 2020-04-09	0.80 (0.077)	0.69 (0.075)	0.55 (0.065)
OS 2020-04-16	0.86 (0.056)	0.77 (0.060)	0.65 (0.050)
ZE 2020-04-05	0.93 (0.086)	0.84 (0.101)	0.71 (0.075)
ZE 2020-04-10	0.99 (0.073)	0.91 (0.084)	0.78 (0.069)
ZE 2020-04-16	0.85 (0.088)	0.75 (0.070)	0.64 (0.055)

2.6 Glint removal methodology

To retrieve $\rho_{glint}(\lambda)$, we propose first to focus on $X=\rho_{surf}(\lambda_{NIR})$ as a function of $Y= \rho_{surf}(\lambda_{red}) - \rho_{surf}(\lambda_{blue})$ because (1) in the absence of glint ($\rho_{surf} = \rho_w$), a linear relationship, named $Y_r \sim X_r$ hereafter, is expected for a certain turbidity range (typically between 3 to 65 NTU) (red line on Figure 4) and (2) when glint is affecting surface measurements, X and Y (X_i and Y_i on Figure 4) deviate from the $Y_r \sim X_r$ curve (red line in Figure 4) along a line with a slope R (green line in Figure 4) which is defined from spectral band ratios of glint reflectance and which is well different than the slope of $Y_r \sim X_r$. Hence, it is then

possible to retrieve the glint corrected point (X_r, Y_r, Figure 4) from the glint contaminated point (X_i, Y_i, Figure 4) by resolving the following system of equations:

$$\begin{cases} Y_r = a + b.X_r \\ Y_i - Y_r = R.(X_i - X_r) \end{cases} \quad \text{With} \quad \begin{cases} X = \rho_{surf}(\lambda_{NIR}) \\ Y = \rho_{surf}(\lambda_{red}) - \rho_{surf}(\lambda_{blue}) \\ R = GR_{red\ NIR} - GR_{blue\ NIR} \end{cases} \tag{4}$$

Where $GR_{red\ NIR}$ ($GR_{blue\ NIR}$) are the ratio between $\rho_{glint}(\lambda_{red})$ ($\rho_{glint}(\lambda_{blue})$) and $\rho_{glint}(\lambda_{NIR})$ and a and b are the intercept and slope of the relationship $Y_r = \rho_w(\lambda_{red}) - \rho_w(\lambda_{blue})$ as a function of $X_r = \rho_w(\lambda_{NIR})$. However, we can wonder why the Y_r versus X_r relationship is necessary linear for moderately turbid waters and how to define moderately turbid water in this case. It is well known and nicely illustrated by [20] that the relationship between $\rho_w(\lambda_{red})$ (or $\rho_w(\lambda_{green})$ or $\rho_w(\lambda_{blue})$) versus $\rho_w(\lambda_{NIR})$ shows a typical saturation curve with a linear increase for low turbidity and a saturation asymptote at high turbidity. The turbidity threshold for saturation increases for spectral bands ranging from blue to red. In the turbidity range where $\rho_w(\lambda_{blue})$ is saturating but not $\rho_w(\lambda_{red})$, it is then expected to obtain a linear relationship. In practice, the Y_r~X_r relationship has been study for a full turbidity range from the non-glinted image of Pléiades and the linear region has been observed for Y_r ranging between 0.005 and 0.03.

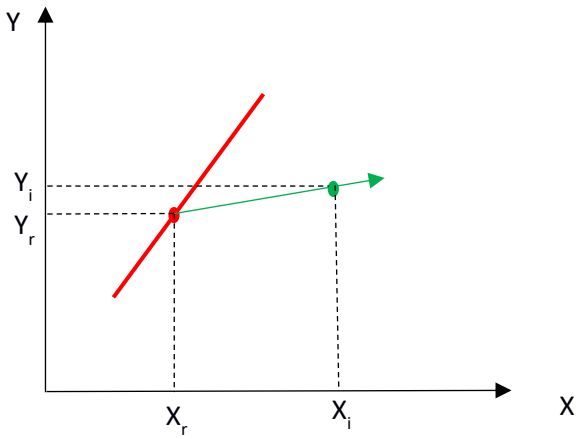

Figure 4. Conceptual figure for glint correction. Red line shows the relationship between X and Y when surface reflectance is not contaminated by glint. Green arrow shows the slope of glint (R).

As Pleiades images in the Belgian coastal waters can show a very high range of turbidity, to be able to process sub-regions with low turbidity or with very high turbidity, alternative functions for the Y_r versus X_r relationships were designed. For low turbidity ρ_w(NIR) is supposed to be constant and close to zero. Then, Y_r is replaced by $\rho_w(\lambda_{red}) - \rho_w(\lambda_{NIR})$ and X_r by $\rho_w(\lambda_{green})$. For very high turbidity, $\rho_w(\lambda_{red})$ is supposed to saturate. Then, Y_r is replaced by $\rho_w(\lambda_{red}) - \rho_w(\lambda_{NIR})$ and X_r by $\rho_w(\lambda_{NIR})$.

Switching decision between these three formations is based on the value of $\rho_w(\lambda_{red}) - \rho_w(\lambda_{NIR})$. If this value is less than 0, low turbidity algorithm is used, whereas if this value is higher than 0.03 high turbidity algorithm is used. If this value is between 0 and 0.005 or between 0.025 and 0.003, both low and medium or high and medium Y_r versus X_r relationships are used respectively. The final value is the average of the both outputs. These thresholds have been defined after careful analysis of the Pleiades images. In practice, $\rho_w(\lambda_{red}) - \rho_w(\lambda_{NIR})$ is calculated for all pixels of the glinted image (Equation (4) and the first estimation of $\rho_w(\lambda_{red}) - \rho_w(\lambda_{NIR})$ is used to determine the Y_r~X_r algorithm. Figure 5 shows the spatial distribution of algorithms estimated from the glinted image of Zeebrugge taken on 2020-04-05.

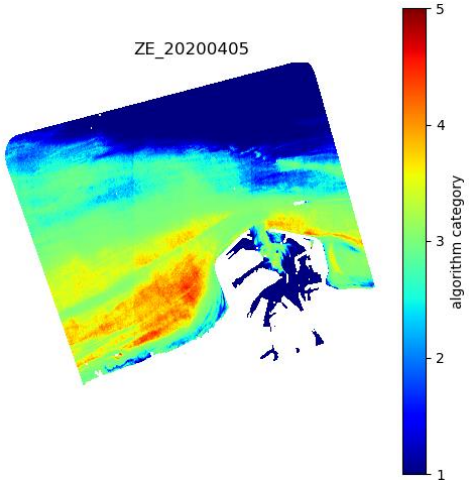

Figure 5. Algorithm model used to retrieve ρ_w. 1 is for low turbidity algorithm, 3 for medium turbidity and 5 for high turbidity. 2 and 4 are for an average between low and medium turbidity algorithm and medium and high turbidity algorithm, respectively. Results are shown for the glinted image of Zeebrugge harbour on 2020-04-16 with extends from 51.30°N to 51.42°N and from 3.06°E to 3.25°E.

In the system of equations (4), a and b are coefficients which are known a priori. It is then necessary to determine them a first time from ancillary information. As the relationship between two spectral bands in the red and near infrared depends mainly on suspended particle properties (size, refraction index, etc., [21]), it is expected that for a given region and season, a and b are constant. However, as CDOM absorption in blue and green is not negligible, in regions showing high CDOM variability, the spatial extent and the temporal range considered to apply a unique set of a and b coefficients may be reduced. a and b can be computed from any glint free water reflectance measurements performed in the study area. Here, we have calculated a and b from standard PANTHYR measurements performed during the period of the glint experiment for PANTHYR data (Figure 6) and from the glint free Pléiades image of Zeebrugge on 2020-04-16 (Figure 7). This image has been chosen because it has a very large range of turbidity and because it is entirely cloud-free. Results are provided in Table 4. In the high turbidity model, the negative slope is close to -1 (Figure 7, right panel, Table 4). This result was expected as $\rho_w(\lambda_{red})$ is assumed to be constant.

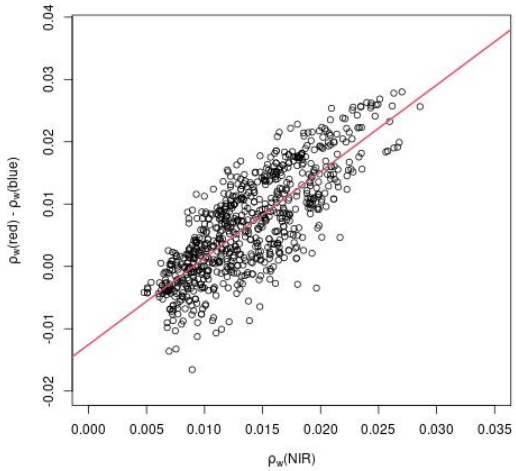

Figure 6: $\rho_w(660) - \rho_w(490)$ as a function of $\rho_w(800)$ from water reflectance measurements made during the PANTHYR sun glint experiment but with the standard protocol.

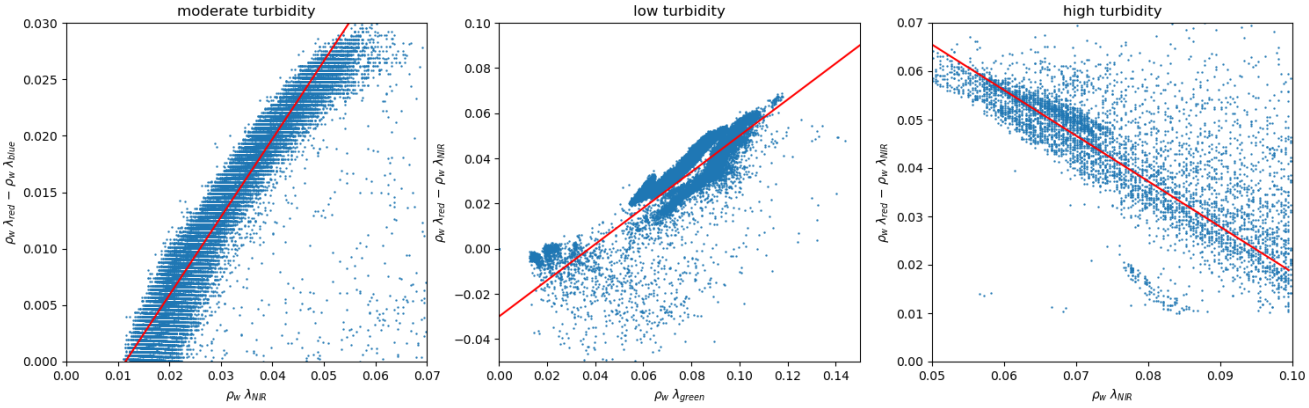

Figure 7. Left: $\rho_w(\lambda_{red}) - \rho_w(\lambda_{blue})$ as a function of $\rho_w(\lambda_{NIR})$ for pixels showing moderate turbidity ($\rho_w(\lambda_{red}) - \rho_w(\lambda_{blue})$ between 0 and 0.03). Middle: $\rho_w(\lambda_{red}) - \rho_w(\lambda_{NIR})$ as a function of $\rho_w(\lambda_{green})$ for pixels showing low turbidity ($\rho_w(\lambda_{red}) - \rho_w(\lambda_{blue})$ less than 0). Right: $\rho_w(\lambda_{red}) - \rho_w(\lambda_{NIR})$ as a function of $\rho_w(\lambda_{NIR})$ for pixels showing high turbidity ($\rho_w(\lambda_{red}) - \rho_w(\lambda_{blue})$ higher than 0.03). Data come from the non-glinted image of Zeebrugge taken on 2020-04-05. Red lines show linear regressions.

Table 4. Intercept (a), slope (b) and coefficient of determination (r^2) calculated from linear regressions performed on Yr~Xr models. Linear regressions are shown in Figure 6 and Figure 7. For PANTHYR data only one relationship could be calculated because of the small turbidity range of the data.

dataset	**$\rho_w(\lambda_{red}) - \rho_w(\lambda_{blue}) \sim \rho_w(\lambda_{NIR})$**	**$\rho_w(\lambda_{red}) - \rho_w(\lambda_{NIR}) \sim \rho_w(\lambda_{green})$**	**$\rho_w(\lambda_{red}) - \rho_w(\lambda_{NIR}) \sim \rho_w(\lambda_{NIR})$**
Pléiades	b=0.69, a=-0.001, r^2=0.95	b=0.80, a=-0.03, r^2=0.96	b=-0.94, a=0.112, r^2=0.79
PANTHYR	b=1.39, a=-0.013, r^2=0.62	-	-

3 RESULTS

3.1 In situ measurements with PANTHYR

The glint removal algorithm has been tested on in situ PANTHYR data and first results confirm the validity of the method. Indeed, on Figure 8, crosses of a same color show the ρ_{surf} measurements from a same measurement cycle and the plain dot of the same color is the corresponding ρ_w value obtained from the PANTHYR standard protocol ($\rho_{w\ SP}$). Crosses of a same color are aligned along relatively parallel lines suggesting that glint ratio between spectral bands is quite similar from one observation date and time to another. The principle of the glint removal methodology is then to extent these glint lines up to the Y_r versus X_r line represented here by the cloud of grey dots. Whereas the five cycles displayed in Figure 8 for illustration of the methodology, seems to validate the approach, a formal evaluation of the retrieval of water reflectance from glinted measurements is provided in Figure 9. Results show that this methodology was very efficient to retrieve red water reflectance ($\rho_w(650)$) as the median absolute percent difference is only 6.8%, the points are well aligned along the 1:1 line with a coefficient of determination of 74%. For $\rho_w(800)$ a slight underestimation is observed especially for low $\rho_w(800)$ NIR although results are acceptable (MAPD is about 30%). This could be due to the higher variability around the Y_r~X_r model for low $\rho_w(800)$ values (Figure 6). Finally, considering that ρ_{glint} is much greater than ρ_w in the PANTHYR glint dataset, the evaluation of ρ_{glint} retrieval gives very positive results.

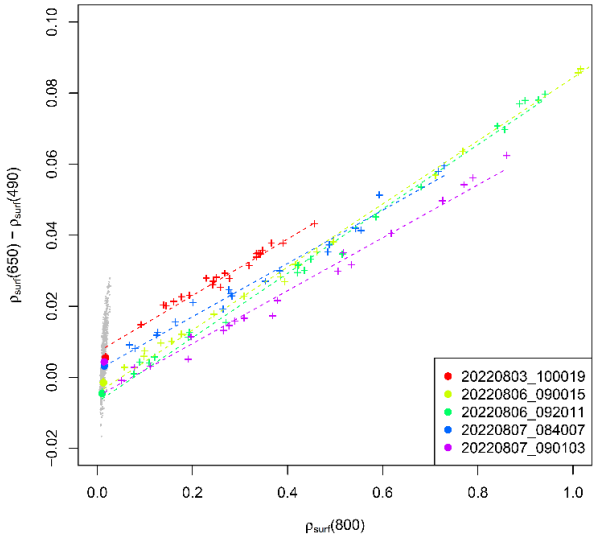

Figure 8. Crosses show $\rho_{surf}(650) - \rho_{surf}(490)$ as a function of $\rho_{surf}(800)$. Filled circles show the same for ρ_w and grey dotted points show ρ_w relationship but for all ρ_w measurements from standard protocol. Color refers to cycle. For visibility only 5 cycles are provided as an example.

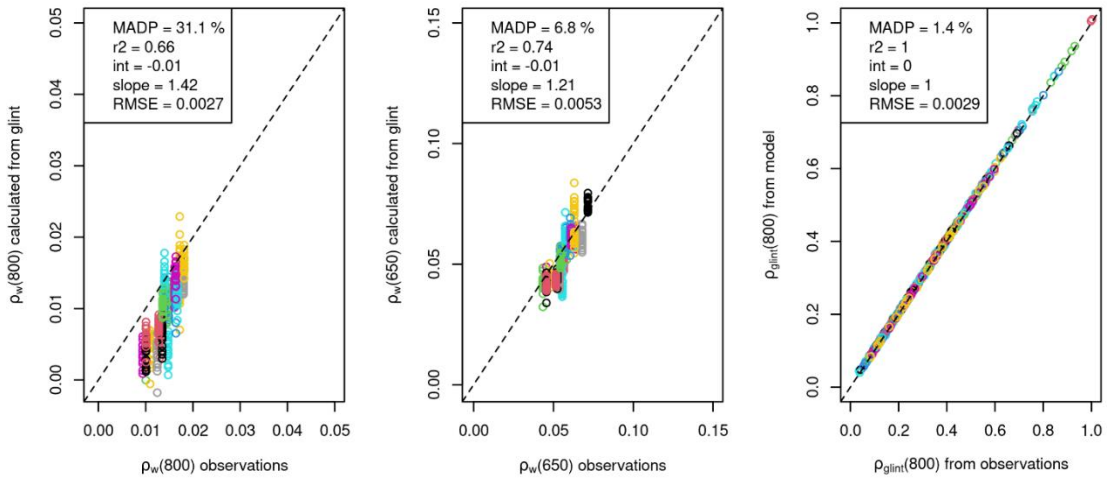

Figure 9. Validation of the glint correction algorithm. x axis is for standard non-glinted PANTHYR observations and y axis for retrieval water reflectance (left and middle panels) and glint reflectance (right panel)

3.2 Pleiades sun glint correction

The sun glint correction algorithm was also tested on Pleiades glinted images and the glint corrected image have been compared to the colocalized non-glinted image. Results (Table 5) show rather good retrieval for visible bands although an overall overestimation is observed in all images except for Ostend 2020-04-05. The analysis of the interquartile range of the percent difference (PD) indicates that for visible bands at least half of the glint corrected pixels show an error lower than 20%. Only the image Zeebrugge 2020-04-16 shows a larger range. The image from Zeebrugge on 2020-04-05 which has been used to calculate a and b coefficients (Table 5) shows very good results, but for visible bands, results are even better for the image Ostend 2020-04-16 which confirms that the Y_r~X_r relationship can be developed from ancillary data from a same region and season. Percentage difference for the NIR band shows much larger interquartile range. This large variability can be explained by the very low values of ρ_w(NIR) but also by algorithm limitations as also observed with PANTHYR data (Figure 9, left panel).

Figure 10 and Figure 12 allow to compare non-glinted $\rho_w(\lambda_{red})$ and glint corrected $\rho_w(\lambda_{red})$ images. It is interesting to see that the very simple glint correction algorithm allows to retrieve main water reflectance spatial structures whereas $\rho_{glint}(\lambda_{red})$ display typical structures of glint like wavelets of any features caused by the wind on the sea surface. However, when focusing on small scale (Figure 11) one can notice that the very high-resolution patterns of the non-glinted image are lost after glint correction. This could be due to small-scale variability around the Y_r-X_r relationship.

Table 5. First quartile, median and third quartile of the percent difference (PD, %) between the glint corrected image and the colocalized glint free image.

ID	**PD (%) (blue)**	**PD (%) (green)**	**PD (%) (red)**	**PD (%) (NIR)**
Ostend 2020-04-16	-32, 3.5, 11.0	-2.3, -1.4, 6.4	-14.3, 0.4, 16.0	-121, -64, -8.4
Zeebrugge 2020-04-05	1.4, 5.5, 10.0	1.8, 6.0, 10.2	2.5, 8.9, 16.8	4.3, 24.0, 62.6
Ostend 2020-04-09	10.8, 15.1, 20.7	7.8, 11.1, 15.0	8.6, 14.7, 22.9	2.2, 24.0, 56.2
Zeebrugge 2020-04-16	3.1, 17.4, 33.2	0.9, 9.3, 19.2	-14.2, 10.5, 43.6	-68.1, -18.0, 48.2
Zeebrugge 2020-04-10	8.3, 13.7, 19.3	7.0, 10.9, 14.8	8.6, 16.6, 25.2	42.5, 82.0, 136

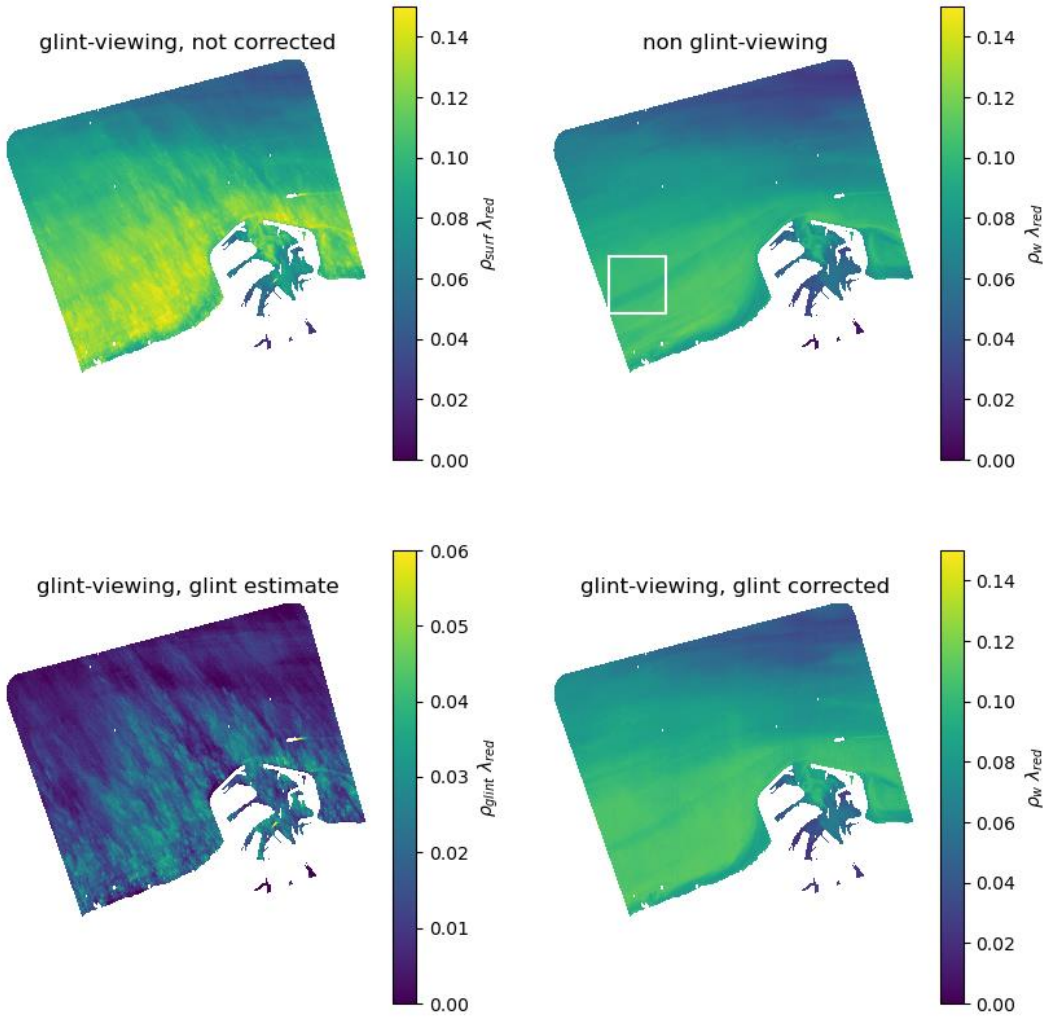

Figure 10. Top panels show the surface reflectance of the red spectral band in the glinted (right) and non-glinted (left) images of Zeebrugge harbour taken on 2020-04-16. In bottom left panel, color scale shows ρ_{glint} distribution and in the right panel the glint corrected water reflectance is shown. This image extends from 51.30°N to 51.42°N and from 3.06°E to 3.25°E

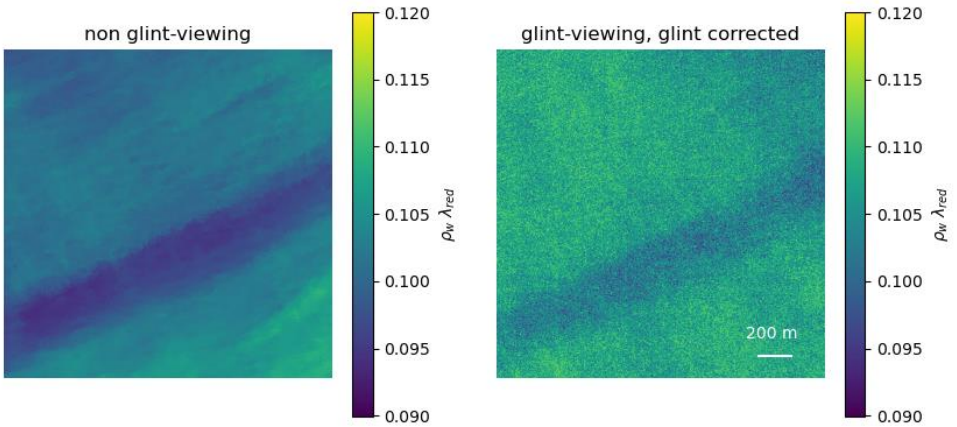

Figure 11. Subset (see white square in) of the water reflectance from non-glinted image (left) and glint corrected water reflectance (right). Subset is from the images of Zeebrugge taken on 2020-04-05 (). Note the colour scale difference with respect to Figure 10.

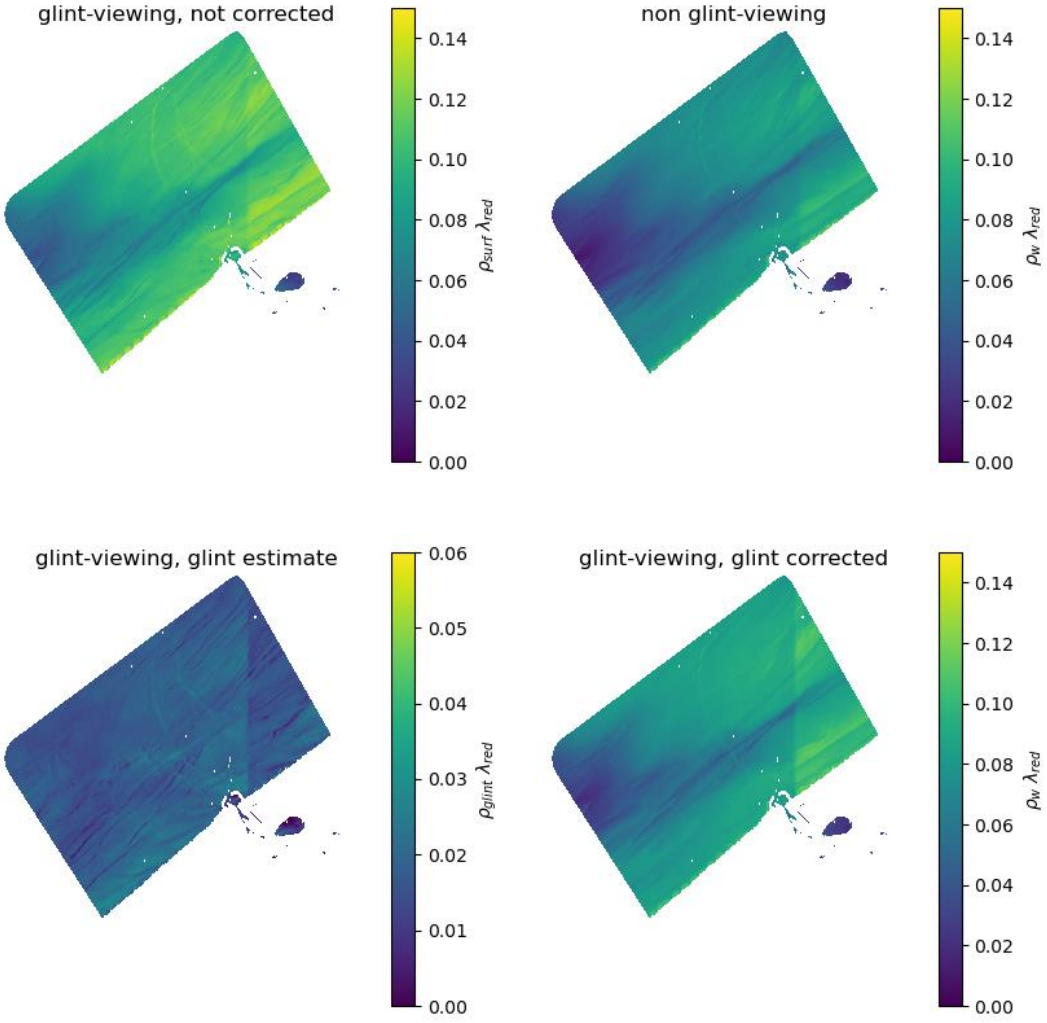

Figure 12. Same as but for the image of Ostend harbour taken on 2020-04-16. This image extends from 51.17°N to 51.32°N and from 2.79°E to 2.30°E

3.3 Limitations and advantages of the present methodology.

A simple and robust methodology is presented here to deglint very high-resolution imagery of turbid waters. This methodology allows to process moderate to very high turbidity waters without a SWIR band. Indeed, most of the deglinting algorithms assume that NIR or SWIR water reflectance is zero or constant and minimum [3]. However, in high turbid waters, water leaving reflectance is variable in NIR and the SWIR should be used [8]. When the SWIR spectral band is not available as it is the case for very high-resolution sensors like Pléiades or Planetscope constellations, the methodology presented still allows to correct for glint. The present methodology is based on two principles: (1) glint reflectance ratio between spectral bands are constant over a small image and can be calculated from the glinted image and (2) there are known and robust relationships between water leaving reflectance at different spectral bands.

The first assumption is often used in glint correction models for high resolution sensors although methodologies to retrieve glint reflectance ratio between spectral bands vary. For instance, [7] or [22] proposed to use clear water pixels to calculate this slope. This requires a pre-examination of the image and can hinder automatic processing. In the present method, a macro-pixel is used and it is assumed that water reflectance is constant within this macro-pixel but glint reflectance is sufficiently variable. Quality control made on the coefficient of determination of the regression allows to ensure that the assumption is true (homogeneous water reflectance) but also that glint variability within pixels is high enough to derive a robust ratio. This method does not require any prior information about the image and is designed for automatic processing. Processing time is regulated by the number of macro-pixels processed. Indeed, it is not necessary to process all the image and some pixels can be skipped.

The second basis of the methodology is the prior knowledge on water reflectance relationships between spectral bands e.g. [23], these models can slightly deviate from one region to another or from one season to another as modifications in the particle properties (size, shape, refraction index, etc.) impact water optical properties and water reflectance [21]. The calculation of a and b coefficients used in Equation (4) then requires a specific analysis of local water reflectance datasets from in situ or satellite data. It is advisable to use satellite data because they generally cover larger turbidity ranges and to use in situ data for their validation. As illustrated in this paper, in situ data can be constrained to smaller turbidity ranges. The thresholds coefficients used in this paper to switch between the different algorithms (low, medium and high turbidity) can also be re-assessed for each study region. The analysis of the a and b coefficients then becomes an important work as it is needed to check the robustness of these coefficients over different special and temporal extents. However, it can be done only once to produce a unique seasonal climatology used to process many images.

The present methodology can only be applied to high resolution sensors, to ensure enough inter-pixel glint variation in the macro-pixel when calculating the glint reflectance ratio between spectral bands, and to turbid waters because of the assumptions on water reflectance saturation schemes. Indeed, the method should not be used for pixels showing macro-algae, surface scum or bottom reflectance. In clear waters, this methodology is also expected to give poor results and other methods assuming null reflectance in NIR should be preferred. However, the present method allows to fill a gap as to our knowledge there was not glint correction model dedicated to high turbidity water for images from very high-resolution sensors without a SWIR band such as Pléiades and Planetscope constellation.

4 CONCLUSION

A new approach is presented to correct glint in turbid waters from images taken by very high-resolution sensors without a SWIR band. The methodology has been tested from two datasets: (1) in situ multi-angle measurements of surface reflectance collected with a PANTHYR autonomous hyperspectral radiometer deployed near Ostend, and (2) a set of metre-scale Pléiades stereo imagery taken in the Belgian coastal zone, with one image of the stereo pair looking into the sun glint and one looking away from the sun glint. Present methodology is based on the combinations of spectral bands for which a linear relationship is observed in water reflectance, and a constant band ratio for glint reflectance directly calculated from the glinted image. To be adapted to a high range of turbidity conditions, a switching approach between band combinations is proposed. Glint removal correction was successfully applied in association with the ACOLITE Dark Spectrum Fitting (DSF) atmospheric correction. Results show a good performance in terms of glint removal, and the average overestimation is reduced to less than 20 % for more than 75% of the pixels in visible bands. Although regional

prior information on water reflectance relationship between spectral bands is needed, the present approach could be easily automatized as images are processed in a very short period of time.

The methodology has been developed and tested for Pléiades constellation but it is applicable to any high-resolution sensor with or without SWIR band.

5 AKNOWLEDGEMENTS

This work has been funded by BELSPO through the Research programme for earth observation STEREO III AQUALOOKS project (contract nr SR/00/374). The Belgian Pléiades Archive is thanked for distribution and acquisition of the images used in this work. We are very grateful to the European Space Agency (ESA) for supporting the PANTHYR data processing under the HYPERNET-VN project. The Flemish Marine Institute (VLIZ) and POM West-Vlaanderen are thanked for operating the PANTHYR on the RT1 Blue Innovation Platform (Ostend, Belgium) and installation support.

REFERENCES

[1] E. J. Hochberg, S. Andréfouët, and M. R. Tyler, "Sea surface correction of high spatial resolution Ikonos images to improve bottom mapping in near-shore environments," *IEEE transactions on geoscience and remote sensing*, vol. 41, no. 7, pp. 1724–1729, 2003.

[2] F. Steinmetz, P.-Y. Deschamps, and D. Ramon, "Atmospheric correction in presence of sun glint: application to MERIS," *Opt. Express*, vol. 19, no. 10, pp. 9783–9800, 2011.

[3] S. Kay, J. D. Hedley, and S. Lavender, "Sun glint correction of high and low spatial resolution images of aquatic scenes: A review of methods for visible and near-infrared wavelengths," *Remote Sens (Basel)*, vol. 1, no. 4, pp. 697–730, 2009.

[4] C. Cox and W. Munk, "Measurement of the roughness of the sea surface from photographs of the sun's glitter," *Josa*, vol. 44, no. 11, pp. 838–850, 1954.

[5] M. Wang and S. W. Bailey, "Correction of sun glint contamination on the SeaWiFS ocean and atmosphere products," *Appl Opt*, vol. 40, no. 27, pp. 4790–4798, 2001.

[6] L. Bourg, F. Montagner, V. Billat, and S. Belanger, "MERIS ATBD 2.13 sun glint flag algorithm," *MERIS IPF*, vol. 6, 2011.

[7] J. D. Hedley, A. R. Harborne, and P. J. Mumby, "Simple and robust removal of sun glint for mapping shallow-water benthos," *Int J Remote Sens*, vol. 26, no. 10, pp. 2107–2112, 2005.

[8] T. Harmel, M. Chami, T. Tormos, N. Reynaud, and P.-A. Danis, "Sunglint correction of the Multi-Spectral Instrument (MSI)-SENTINEL-2 imagery over inland and sea waters from SWIR bands," *Remote Sens Environ*, vol. 204, pp. 308–321, 2018.

[9] T. Kutser, E. Vahtmäe, and J. Praks, "A sun glint correction method for hyperspectral imagery containing areas with non-negligible water leaving NIR signal," *Remote Sens Environ*, vol. 113, no. 10, pp. 2267–2274, 2009.

[10] D. Vansteenwegen, K. Ruddick, A. Cattrijsse, Q. Vanhellemont, and M. Beck, "The pan-and-tilt hyperspectral radiometer system (PANTHYR) for autonomous satellite validation measurements—Prototype design and testing," *Remote Sens (Basel)*, vol. 11, no. 11, p. 1360, 2019.

[11] Q. Vanhellemont and K. Ruddick, "Atmospheric correction of Sentinel-3/OLCI data for mapping of suspended particulate matter and chlorophyll-a concentration in Belgian turbid coastal waters," *Remote Sens Environ*, vol. 256, p. 112284, 2021.

[12] H. Lavigne, K. Ruddick, and Q. Vanhellemont, "Monitoring of high biomass Phaeocystis globosa blooms in the Southern North Sea by in situ and future spaceborne hyperspectral radiometry," *Remote Sens Environ*, vol. 282, p. 113270, 2022.

[13] K. G. Ruddick, V. De Cauwer, Y.-J. Park, and G. Moore, “Seaborne measurements of near infrared water-leaving reflectance: The similarity spectrum for turbid waters,” *Limnol Oceanogr*, vol. 51, no. 2, pp. 1167–1179, 2006.

[14] S. Q. Duntley, R. W. Austin, W. H. Wilson, C. F. Edgerton, and S. E. Moran, “Ocean color analysis,” *SIO Ref*, vol. 7410, no. 1, p. 1, 1974.

[15] C. D. Mobley, “Estimation of the remote-sensing reflectance from above-surface measurements,” *Appl Opt*, vol. 38, no. 36, pp. 7442–7455, 1999.

[16] P. Gege and P. Grötsch, “A spectral model for correcting sunglint and skyglint,” *Proceedings of Ocean Optics XXIII 2016*, pp. 1–10, 2016.

[17] Q. Vanhellemont and K. Ruddick, “Atmospheric correction of metre-scale optical satellite data for inland and coastal water applications,” *Remote Sens Environ*, vol. 216, pp. 586–597, 2018.

[18] Q. Vanhellemont, “Adaptation of the dark spectrum fitting atmospheric correction for aquatic applications of the Landsat and Sentinel-2 archives,” *Remote Sens Environ*, vol. 225, pp. 175–192, 2019.

[19] H. R. Gordon, J. W. Brown, and R. H. Evans, “Exact Rayleigh scattering calculations for use with the Nimbus-7 coastal zone color scanner,” *Appl Opt*, vol. 27, no. 5, pp. 862–871, 1988.

[20] Y. Luo *et al.*, “Saturation of water reflectance in extremely turbid media based on field measurements, satellite data and bio-optical modelling,” *Opt Express*, vol. 26, no. 8, pp. 10435–10451, 2018.

[21] M. Babin, A. Morel, V. Fournier-Sicre, F. Fell, and D. Stramski, “Light scattering properties of marine particles in coastal and open ocean waters as related to the particle mass concentration,” *Limnol Oceanogr*, vol. 48, no. 2, pp. 843–859, 2003.

[22] D. R. Lyzenga, N. P. Malinas, and F. J. Tanis, “Multispectral bathymetry using a simple physically based algorithm,” *IEEE Transactions on Geoscience and Remote Sensing*, vol. 44, no. 8, pp. 2251–2259, 2006.

[23] B. Nechad, K. G. Ruddick, and Yjrs. Park, “Calibration and validation of a generic multisensor algorithm for mapping of total suspended matter in turbid waters,” *Remote Sens Environ*, vol. 114, no. 4, pp. 854–866, 2010.